SCIENCE CHINA
Information Sciences

• RESEARCH PAPER •

July 2026, Vol. 69, Iss. 7, 170406:1–170406:11
https://doi.org/10.1007/s11432-026-4987-2

Special Topic: Advanced Optoelectronics Based on Two-Dimensional Materials

A platform of MoS_2/4H-SiC heterostructure photonic synapses for low-power neuromorphic machine vision

Gaotian ZHANG[1], Ruoyao SUN[1], Yining GONG[2], Sina LI[3], Mengmeng YANG[1], Xiao LIU[1], Dongxiang LUO[4], Xingfu WANG[1*], Feng ZHANG[5*] & Wei GAO[1*]

[1]*Guangdong Provincial Key Laboratory of Chip and Integration Technology, School of Electronic Science and Engineering (School of Microelectronics), Faculty of Engineering, South China Normal University, Foshan 528200, China*
[2]*International Business College, South China Normal University, Foshan 528200, China*
[3]*School of Optoelectronic Engineering, Guangdong Polytechnic Normal University, Guangzhou 510665, China*
[4]*Huangpu Hydrogen Innovation Center, School of Chemistry and Chemical Engineering, Guangzhou University, Guangzhou 510665, China*
[5]*Department of Physics, Xiamen University, Xiamen 361005, China*

Received 15 March 2026/Revised 22 April 2026/Accepted 4 June 2026/Published online 22 June 2026

Abstract Optoelectronic synapse devices hold enormous application prospects in neuromorphic machine vision but suffer from critical challenges including heteroepitaxial lattice mismatch and cumbersome fabrication processes. 4H-SiC offers distinct merits for high-performance neuromorphic devices due to its wide bandgap, high defect tolerance, and CMOS compatibility. Herein, we fabricated ultra-low-power photonic synapses based on MoS_2/4H-SiC heterostructures, realizing faithful emulation of biological visual information processing. Under 405-nm illumination (5.05 mW $\cdot$ cm^{-2}), the device exhibited amplified photoresponse with increasing light pulses: excitatory postsynaptic current change (ΔEPSC) rose progressively to saturation, mimicking biological reinforcement learning. It also achieved non-volatile long-term memory, with current remaining stable after light cessation. Pair-pulse facilitation (PPF) experiments showed a peak PPF index of 134.4% at 50 ms pulse interval, followed by exponential decay, consistent with biological short-term potentiation (STP). For handwritten digit recognition, the neural network (784 input, 300 hidden, 10 output neurons) achieved 86% accuracy in cycle 1, 93.7% in cycle 9 (2.3% below ideal), and sustained $>$ 94% accuracy in cyclic testing, verifying superior synaptic durability. This proof-of-concept work lays a solid foundation for integrated 2D/SiC photonic synapses and promotes the development of low-power intelligent information processing systems with future scalable fabrication compatibility.

Keywords MoS_2/4H-SiC heterostructure, neuromorphic devices, biological synapses, non-volatile long-term memory, handwritten digit recognition

Citation Zhang G T, Sun R Y, Gong Y N, et al. A platform of MoS_2/4H-SiC heterostructure photonic synapses for low-power neuromorphic machine vision. Sci China Inf Sci, 2026, 69(7): 170406, https://doi.org/10.1007/s11432-026-4987-2

1 Introduction

The von Neumann architecture's inherent separation of computing and storage units mandates frequent data migration between processors, storage modules, and optical sensing components, giving rise to substantial energy consumption and critical speed bottlenecks that severely impede overall system efficiency. This limitation becomes particularly acute amid the explosive growth in demand for image data processing tasks [1–4]. Neuromorphic computing devices exhibit remarkable energy efficiency advantages by breaking down the separation between storage and computation units, thereby emulating the human brain's highly efficient information processing paradigm. Inspired by the biological retina, neuromorphic visual devices feature high bandwidth, low crosstalk, and fast response modulation. Such devices are designed to replicate the energy-efficient integration of perception, storage, and computation inherent to biological visual systems, paving the way toward next-generation intelligent computing architectures characterized by high-density storage, low power consumption, and efficient information processing [5–8]. A diverse array of optoelectronic neuromorphic devices has been demonstrated to date, including resistive switching memories based on InGaP/HfO_2 [9] and TiO_2/SiO_2 stacked dielectric heterostructures phase-change memory (PCM) [10], ferroelectric field-effect transistors, and ion-modulated electric double-layer transistors [11]. These devices enable dynamic modulation of synaptic weights, thereby supporting highly parallel, adaptive, and low-power information processing paradigms. However, conventional optoelectronic synapses are predominantly reliant

* Corresponding author (email: xfwang@scnu.edu.cn, fzhang@xmu.edu.cn, gaowei317040@m.scnu.edu.cn)

on heterostructured material architectures, which impose three intrinsic limitations. (i) Crystallographic lattice mismatch: lattice misalignment at heterogeneous material interfaces engenders strain-induced defect formation. (ii) Interface degradation: surface dangling bonds give rise to high trap state densities, which in turn induce Fermi-level pinning and non-radiative recombination-related energy losses. (iii) Fabrication complexity: multi-step deposition and etching processes not only complicate device manufacturing but also compromise the reproducibility of the final devices [12, 13]. These challenges underscore the urgent need to develop novel-structured optoelectronic synaptic device-integrated systems in which both photodetection and synaptic functionalities derive from engineered bulk material properties rather than interfacial effects. This structural design is poised to eliminate heterointerface-associated constraints while enabling wafer-scale integration through CMOS-compatible fabrication processes.

Two-dimensional (2D) materials represent an ideal platform for fabricating high-performance optoelectronic synaptic devices, owing to their atomically flat interfaces, tunable electrostatic characteristics, facile integration protocols, and exceptional light-matter interaction capabilities. Through the rational construction of heterostructures, the synergistic merits of diverse 2D materials in layer stacking and physical property modulation can be fully harnessed, thereby greatly expanding the functional application prospects of such devices [14,15]. Notably, leveraging these exceptional inherent properties, extensive investigations have been carried out to date into the application of optoelectronic synapses. For instance, the ferroelectric polarization of In_2Se_3 enables the emulation of synaptic behaviors, yet practical implementation remains impeded by hurdles including cumbersome optoelectronic function coordination, structural intricacy, and operational limitations confined to the visible light spectrum [16–18]. For its part, MoS_2 allows for faithful emulation of complex neural dynamics in memristive devices, while few-layer SnSe/MoS_2 van der Waals heterojunctions deliver highly efficient optoelectronically synergistic synaptic functionalities. These advances collectively broaden the application horizons of 2D material-based devices in optoelectronic neuromorphic systems [19]. Nevertheless, despite the exceptional properties that render MoS_2 a highly promising candidate for neuro-optoelectronic synaptic devices, a number of intractable challenges remain unresolved. These include the sophisticated fabrication process that relies on the chemical vapor deposition (CVD) technique, relatively limited synaptic retention durations, and suboptimal synaptic response efficiency in the visible light spectrum.

Notably, silicon carbide (SiC) serves as an ideal material platform for constructing highly stable, low-power neuromorphic devices, thanks to its inherent characteristics, including a high critical breakdown field, superior electron saturation velocity, and exceptional thermal conductivity [20–22]. In synaptic device applications, SiC facilitates the sustained modulation of photogenerated carriers via defect engineering tailored to regulate charge capture and release dynamics, thereby emulating the short- and long-term plasticity inherent to biological synapses [23,24]. Shen et al. [25] fabricated photonic synaptic devices based on SiC@NiO core-shell nanowire networks, which exhibited tunable synaptic plasticity and neuromorphic functionalities with photosensitive synergistic effects. A high-temperature ultraviolet light (UV) photoconductive synaptic device built on a p-n 4H-SiC homojunction maintains reliable light-modulated synaptic behaviors and image learning-memory capabilities at 350°C even without encapsulation. This device attains a 95% accuracy rate in handwritten digit recognition via neural network integration, thus offering a robust solution for neuromorphic computing applications under high-temperature harsh conditions [26]. These advances underscore SiC's great potential in integrated photonic neuromorphic systems that integrate sensing, storage, and computing functions, thereby opening up a novel material pathway to address the energy efficiency bottlenecks inherent in traditional von Neumann architectures. Overall, by synergizing SiC's superior visible-light synaptic response and ultra-long retention duration with MoS_2's low-power consumption and excellent optoelectronic sensitivity, we aim to develop high-performance, low-power optoelectronic synergistic synaptic devices. Nevertheless, the interfacial issues pertaining to the heterojunction structures mentioned above remain a key limiting factor.

Herein, we innovatively adopt MoS_2 as the electron transport channel. The introduced SiO_2 isolation layer serves to separate the electrode from the SiC substrate and block direct electrical contact between them. In stark contrast to conventional heterojunction designs, SiC is exclusively engineered as an optically sensitive electron-trapping layer to modulate interfacial electron transfer dynamics, while being fully isolated from the main current conduction pathway. Through this rationally devised architecture, we have successfully fabricated a high-performance optoelectronic synaptic device with inherent low-power-consumption characteristics. Under 405 nm illumination, the device exhibits exceptional photoresponse capabilities; experimental validation via pulse-coded optical excitation further confirms its conformity to fundamental synaptic plasticity paradigms, including paired-pulse facilitation (paired-pulse facilitation (PPF) coefficient: 134.4% at an inter-pulse interval $\Delta t = 50$ ms) and long-term potentiation (retention duration exceeding 120 s). The device faithfully simulates core biological synaptic behaviors-encompassing short-/long-term plasticity and paired-pulse facilitation-while demonstrating robust multi-level storage capability and high operational durability. Systematic material characterization reveals a type-I band alignment configuration and defect-mediated charge capture/release dynamics at the heterojunction interface, which provide a solid

physical basis for the observed photonic synapse functionality. Subsequent neural network simulation experiments utilizing the device achieve a 93.7% recognition accuracy in the Modified National Institute of Standards and Technology (MNIST) handwritten digit classification task, validating its great potential for deployment in low-power, highly integrated neuromorphic computing systems. Collectively, these results establish a reliable proof-of-concept device platform for advancing next-generation intelligent systems integrating in-memory computing and perception-processing capabilities, while pioneering promising new avenues for 2D semiconductor/wide-bandgap semiconductor heterojunctions in the burgeoning field of neuromorphic optoelectronics. We fully recognize that mechanical exfoliation is not suitable for large-scale wafer-level manufacturing; thus, this proof-of-concept demonstration provides a viable pathway for future wafer-scale integration through CVD-grown large-area MoS_2 films.

2 Results and dissusion

In the biological visual system, the eye serves as the core sensory organ, receiving external light stimuli via the retina and converting them into electrochemical signals. These signals are subsequently interpreted by the brain to form visual images. This process relies on the coordinated action of the nervous system, wherein synapses play a pivotal role in the preprocessing of visual information. They achieve plastic regulation of visual signals by modulating the strength of connections between presynaptic and postsynaptic neurons-that is, synaptic weights [27–29]. Inspired by this mechanism (Figure 1(a)), this study designed and constructed a photoelectric synapse device based on a MoS_2/4H-SiC heterojunction (Figure 1(b)) to mimic the functional characteristics of the biological visual system. Within this device, applied photons or electrical pulses serve as presynaptic inputs, with drain current corresponding to postsynaptic responses. Changes in channel conductance reflect the regulation process of synaptic weights. Device fabrication commenced with the thermal oxidation of an epitaxially grown 4H-SiC substrate to form a SiO_2 dielectric layer, followed by stacking of mechanically exfoliated MoS_2 nanosheets for heterojunction construction. Subsequently, source, drain, and gate electrodes were patterned and deposited via metal evaporation. Figure 1(c) displays a high-resolution transmission electron microscopy cross-sectional image of the heterojunction, clearly revealing the flatness and structural integrity of the MoS_2/4H-SiC interface. Figure 1(d) further validates the distinct components and sharp interfaces of MoS_2, SiO_2, and 4H-SiC through elemental distribution maps (Mo, S, O, Si, and C), confirming the successful construction of the heterostructure. (The complete Scanning Electron Microscopy (SEM) mapping of this device is provided in Figure S1.) The characteristics of the MoS_2/4H-SiC heterostructure were systematically analyzed using multiple techniques. Observations via an Atomic Force Microscope (AFM) (Figure 1(e)) revealed a thickness of 62 nm for multilayered MoS_2 on the 4H-SiC. Notably, as shown in Figure 1(f), the Raman spectrum of pristine MoS_2 exhibits characteristic vibration peaks: the E_{2g} mode at 383.9 cm^{-1} and the A_{1g} mode at 410.2 cm^{-1}. Meanwhile, the heterostructure retains the phonon modes of 4H-SiC, with the E_2(TO) mode at 778.9 cm^{-1} and A_1(LO) mode at 986.2 cm^{-1} clearly identifiable. Furthermore, the Raman spectrum confirms a high degree of crystalline uniformity across the entire SiC/MoS_2 heterostructure, collectively verifying that the intrinsic characteristic peaks of both pristine MoS_2 and 4H-SiC are retained following heterostructure fabrication [30–32]. Additionally, as presented in Figure S2, the Raman spectrum of the SiC/MoS_2 heterostructure in the 100–300 cm^{-1} wavenumber range exhibits distinct features. Specifically, the longitudinal acoustic (LA) phonon mode of MoS_2 is distinctly observed at 207 cm^{-1}, a result consistent with the defect-related LA mode characteristics of MoS_2 documented in prior studies [33]. Furthermore, as depicted in Figure 1(g), photoluminescence (PL) spectroscopy with an excitation wavelength of 295 nm reveals an emission peak at 395 nm for 4H-SiC, corresponding to an intrinsic indirect bandgap of 3.14 eV [34]. Additionally, the appearance of broad PL emission peaks at 433 and 513 nm under the same 295 nm excitation indicates the presence of intrinsic defects within the 4H-SiC substrate, which further rationalizes the optoelectronic synaptic responses observed under visible-light irradiation [35]. Building on this experimental evidence, we propose that the intrinsic defects in both SiC and MoS_2 underpin the synaptic functionality by mediating electron trapping and release processes.

In neuromorphic computing, synaptic plasticity serves as the core mechanism for simulating biological learning and memory processes, wherein short-term plasticity (STP) and long-term plasticity (LTP) are regarded as the fundamental basis for information processing and transmission in artificial neural networks [36,37]. This study systematically modulated multiple parameters-including light power density (P), pulse frequency, and pulse duration-to validate the reconfigurable synaptic properties. Figure 2(a) presents the photoresponse curves under varying light power densities (P). Upon illumination, photogenerated carriers are rapidly generated and separated within the MoS_2/4H-SiC heterojunction, leading to a gradual increase in the device current. When the light is turned off, sustained injection of trapped carriers from the shallow defect levels in 4H-SiC into the MoS_2 channel results in a slow decay of the dark current, which prevents the current from rapidly recovering to its initial state. As illus-

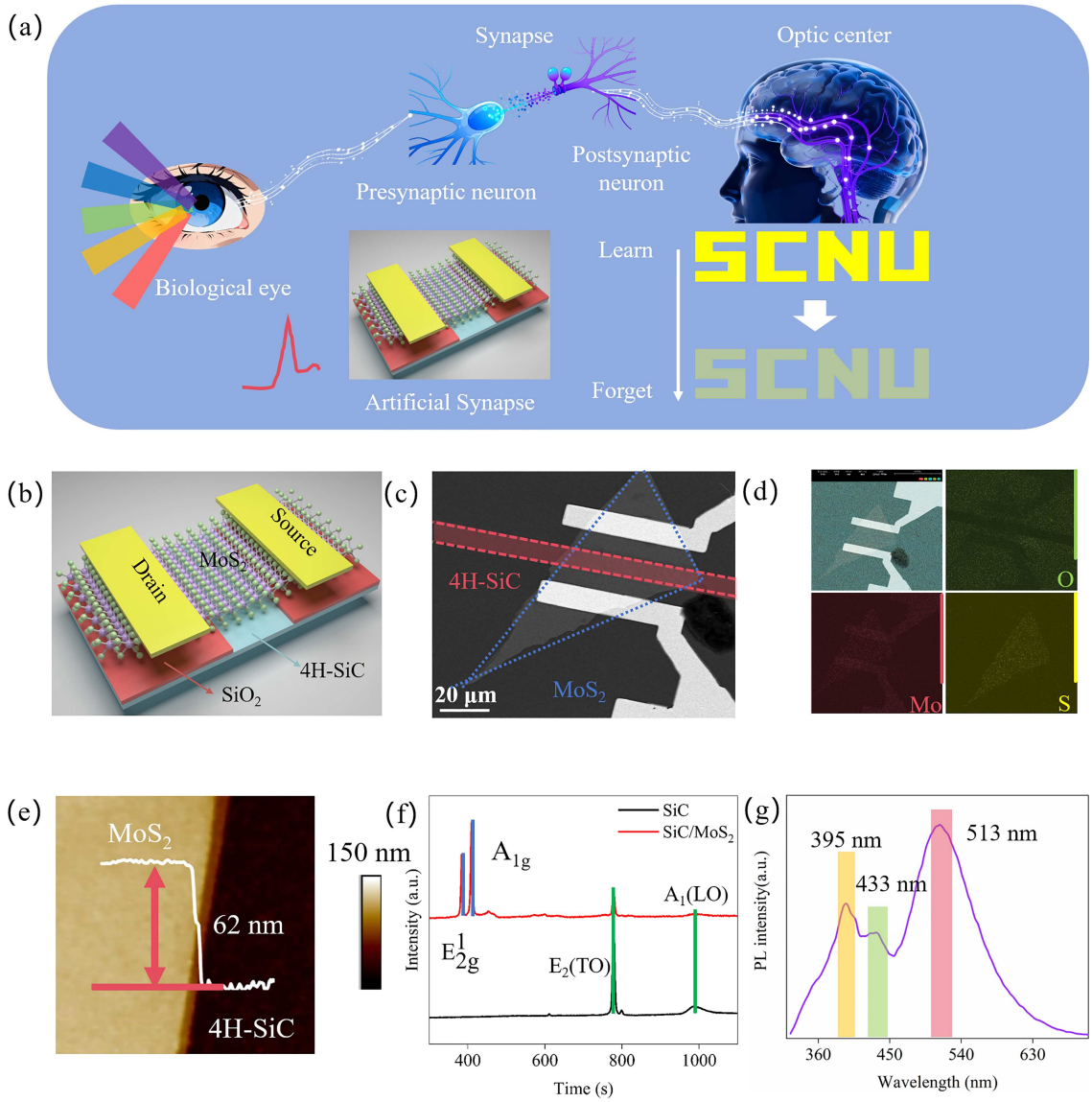

Figure 1 (Color online) (a) Schematic diagram of the visual system and information transmission within the human nervous system. (b) Schematic structure of the MoS_2/4H-SiC heterojunction opto-synaptic device. (c) SEM micrograph of the MoS_2/4H-SiC heterojunction opto-synaptic device. (d) Cross-sectional SEM image of the MoS_2/4H-SiC heterojunction. (e) AFM image, (f) Raman spectrum and (g) photoluminescence spectrum of the MoS_2/4H-SiC device.

trated in Figure 2(b), the photocurrent exhibits a nonlinear dependence on the P, where the normalized excitatory postsynaptic current variation is defined as

$$\Delta\text{EPSC} = (I_{\text{light}} - I_{\text{dark}})/I_{\text{dark}}. \tag{1}$$

This power-dependent current modulation behavior, which directly reflects the tunable excitatory postsynaptic current (EPSC), mimics the plasticity of biological synapses, thus demonstrating the optical tunability of synaptic weights [38]. Figure 2(c) shows that I_{ds} exhibits a monotonically increasing trend as pulse widths increase from 300 ms to 1.5 s, reflecting the gradual strengthening of synaptic weights. For Figure 2(d), the fitting results indicate that ΔEPSC approaches saturation under wide-pulse conditions-this nonlinear behavior is governed by the dynamic equilibrium between the generation and recombination of photogenerated carriers. Figure 2(e) further depicts the nonlinear variation of the drain-source current (I_{ds}) with the number of light pulses under fixed pulse parameters (pulse width: 300 ms; pulse interval: 300 ms). As the number of light pulses increases, both I_{light} and I_{dark} exhibit a gradual increase in amplitude, which mimics the reinforcement mechanism of synaptic functionality in biological neural systems induced by repeated stimulation [39]. Following the cessation of light pulses, the drain-source current (I_{ds}) exhibits a slow decay without recovering to its initial baseline, thereby confirming LTP and

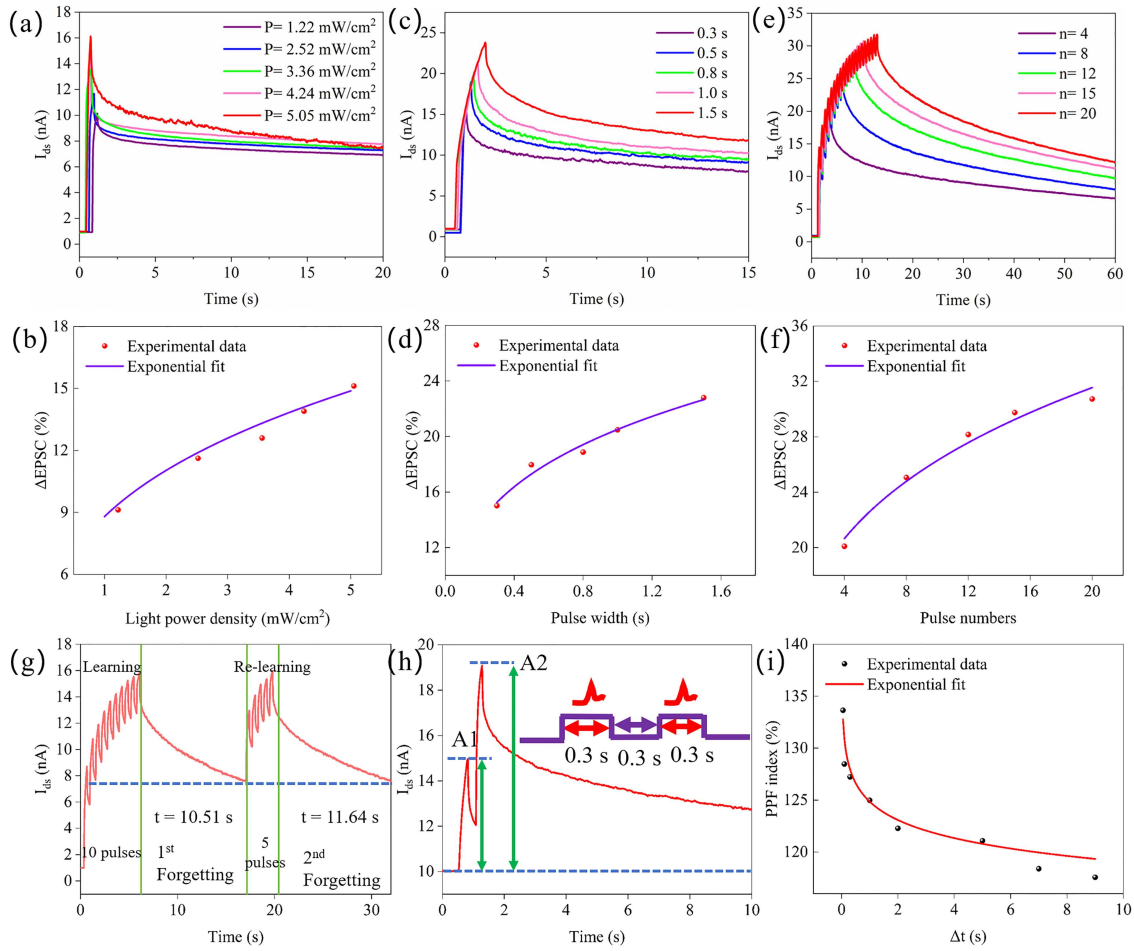

Figure 2 (Color online) (a) Current responses of the device at $V_{ds} = 0.1$ V under varying light power densities of 405 nm. (b) Fitted relationship between ΔEPSC and varying light power densities of the 405 nm laser. (c) Current responses to continuous light pulses (pulse widths ranging from 300 ms to 1.5 s) at 405 nm and $P = 5.05$ mW · cm^{-2} under $V_{ds} = 0.1$ V. (d) Fitted relationship between ΔEPSC and different pulse widths. (e) Current response triggered by optical pulses at $V_{ds} = 0.1$ V, 405 nm wavelength, and a light power density of 5.05 mW · cm^{-2}, for different pulse numbers. (f) Fitted relationship between ΔEPSC and different pulse numbers. (g) "Learning-experience" behavior of the device, including learning, forgetting, and relearning processes. (h) EPSC induced by two consecutive light pulses, used to calculate the PPF index. (i) Variation of the PPF index with pulse interval Δt and its double-exponential fit.

long-term memory (LTM) behaviors. Notably, this phenomenon is likely attributed to the synergistic effect of the pronounced photoconductive response of pristine MoS_2 and intrinsic defect-mediated charge capture/release processes in epitaxial 4H-SiC, which enables the current to be stably maintained at a non-volatile baseline state [40–42]. Figure 2(f) reveals that the ΔEPSC gradually increases with the number of light pulses before eventually saturating, which is consistent with the enhancement of synaptic efficacy through iterative stimulation in biological learning processes. As illustrated in Figure 2(g), the device's I_{ds} exhibits a gradual increase under 10 consecutive light pulse stimuli, which aligns with the characteristic learning process of biological synapses. After the cessation of light pulse excitation, the I_{ds} begins to decay, a behavior consistent with the natural forgetting mechanism of biological synapses. To restore the learning performance to the level attained in the initial learning phase, a second round of continuous light pulse stimulation was applied. Notably, in this relearning stage, merely 5 successive light pulses were sufficient to elevate the I_{ds} to the same amplitude achieved with 10 continuous pulses in the first learning cycle-this finding directly demonstrates the device's robust relearning capability. Moreover, compared to the first forgetting period, the second forgetting process required a significantly longer duration to decay to a comparable I_{ds} level, revealing an improvement in the device's memory retention capability [15]. Collectively, these experimental results bear striking similarities to the learning and memory behaviors observed in the human brain. Furthermore, Figure 2(h) simulates the PPF effect through dual-pulse optical stimulation ($\Delta t = 300$ ms, $V_{ds} = 0.1$ V). It demonstrates that the I_{light} evoked by the second light pulse is significantly amplified relative to the first ($\Delta A = A_2 - A_1$), indicating the presence of a light-flow superposition effect (where A_1 and A_2 are the illuminated I_{ds} from the first and second pulses, respectively). In Figure 2(i), the PPF index (defined as $A_2/A_1 \times 100\%$) [27]

peaks at 134.4% at $\Delta t = 50$ ms, obeying a biexponential relaxation function [43]:

$$\mathrm{PPF} = A_0 + A_1 \mathrm{e}^{-\Delta t/t_1} + A_2 \mathrm{e}^{-\Delta t/t_2}. \tag{2}$$

Fitting analysis yielded two decay time constants for the biexponential function: t_1 (fast phase) = 0.34 s and t_2 (slow phase) = 3.91 s. The fast relaxation component with $t_1 = 0.34$ s arises from rapid detrapping of photogenerated carriers captured at shallow defect states (E_1) in the MoS_2/4H-SiC heterostructure, which enables fast charge recombination and quick recovery of synaptic response. In contrast, the slow decay process with $t_2 = 3.91$ s is dominated by the slow release of electrons trapped in deep defect levels (E_2) within 4H-SiC. These deep defects act as long-term charge-trapping centers, leading to prolonged carrier retention and delayed charge dissipation, which accounts for the slow relaxation behavior of the PPF index [44]. These figures show a high degree of correspondence with the biophysical timeframes associated with PPF attenuation in biological synapses, thereby strongly validating the biomimetic temporal dynamic behaviors [12]. Through multi-parameter modulation, the device achieves systematic emulation of biological synaptic plasticity, showcasing significant application potential in low-power neuromorphic computing and optoelectronically integrated intelligent systems. Notably, both pristine MoS_2 and the MoS_2/SiC heterostructure (tested at 532 and 808 nm) require relatively high driving voltages to manifest synaptic functionalities, as illustrated in Figure S3. In contrast, the MoS_2/SiC heterostructure can realize synaptic functionalities at a low V_{ds} of 0.1 V under 405 nm illumination. Accordingly, all subsequent performance characterizations were performed under 405 nm illumination.

As shown in Figure S4, ultraviolet photoelectron spectroscopy (UPS) and valence band X-ray photoelectron spectroscopy (VB-XPS) characterizations demonstrate that the Fermi level (E_f) of 4H-SiC is −4.3 eV, with its valence band maximum (E_v) and conduction band minimum (E_c) located at −6.74 and −3.6 eV, respectively (detailed calculation procedures are provided in Note S1). For multilayered MoS_2, by contrast, the E_c and E_v are reported to be −4.3 and −5.5 eV in prior literature [45]. Combined with the documented work function of MoS_2 (4.35 eV), a detailed schematic of the band alignment prior to heterojunction contact is illustrated in Figure S5.

As shown in Figure S5, a moderate degree of interfacial band bending is observed: the energy bands of 4H-SiC undergo an upward shift, while those of MoS_2 exhibit a downward tilt. This subtle band bending stems from the intrinsic E_F misalignment between 4H-SiC and MoS_2, which induces partial carrier transfer-specifically, a small population of electrons migrates from 4H-SiC (with a relatively higher E_F) to MoS_2 (with a lower-lying E_F)-until the Fermi levels of the two materials reach a state of equilibrium. This observation thus confirms the formation of a type-I SiC/MoS_2 heterojunction, in good agreement with prior literature reports [46].

Notably, both 4H-SiC and MoS_2 harbor diverse intrinsic defects, consistent with the aforementioned PL and Raman spectroscopy results. These defect states are labeled in the energy band diagram and distinguished by dashed boxes of different colors to ensure clear identification. Specifically, the defect energy levels of 4H-SiC are designated as E_1 (−3.87 eV) and E_2 (−4.32 eV), thereby facilitating the subsequent mechanistic interpretation of optoelectronic synaptic responses.

As illustrated in Figures 3(a)–(c), the device schematic and carrier distribution under dark conditions and under synaptic response conditions are presented. As illustrated in Figure 3(a), under dark conditions with $V_{ds} = 0.1$ V, MoS_2 functions as a conventional electron channel, thus permitting the normal migration of electrons from the source electrode to the drain electrode and the steady current under this state is referred to as I_{dark}. Though intrinsic defects are present in both the MoS_2 layer and the SiC epitaxial film, the direction of the external electric field facilitates the efficient separation of carriers before they are captured by defect states, thereby eliminating detrimental impacts on charge transport.

As illustrated in Figures 3(b) and (d), under 0.1 V bias and illumination, the type-I band alignment facilitates the transfer of photogenerated electrons from the E_C of 4H-SiC to MoS_2, whereas photogenerated holes migrate in the opposite direction to the E_V of 4H-SiC. This enhanced electric field promotes the efficient separation of photoexcited carriers before they are trapped by defect states. Accordingly, I_{light} is primarily dominated by heterojunction-mediated radiative recombination and electron transfer processes that are unaffected by defect trapping.

Notably, as illustrated in Figures 3(c) and (e), at the moment of light termination under 0.1 V bias, the charge carriers (electrons) trapped by the defect energy levels E_1 and E_2 of 4H-SiC (located within the visible-light spectrum) as well as the defect states of MoS_2 during illumination undergo sustained emission over a certain duration. Correspondingly, the photocurrent undergoes a significant decay following light cessation and subsequently stabilizes at a steady-state value that deviates from the initial dark current level. Moreover, the intrinsic photogating effect originating from interface trap states at the SiC/MoS_2 heterojunction promotes electron emission from the aforementioned defect states by suppressing carrier recombination.

As shown in Figure 3(f), to clarify the electron transport behavior across the heterojunction, we measure the single-pulse photocurrent curves of the device under different V_{ds}. Notably, the higher the applied V_{ds}, the longer

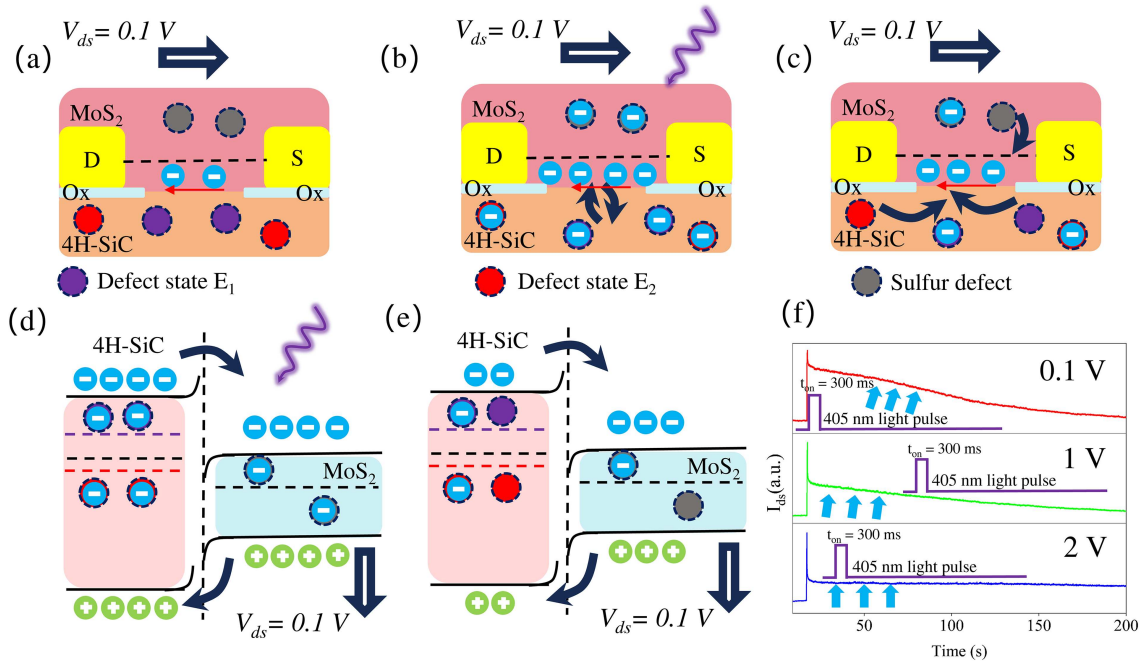

Figure 3 (Color online) Schematic illustrations of device structure and carrier distribution. (a) Under dark conditions; (b) under light illumination; (c) after illumination; (d) band diagram of SiC/MoS_2 under illumination at V_{ds} = 0.1 V; (e) band structure diagrams of SiC/MoS_2 after illumination; (f) current response response at 405 nm and $P = 5.05\ \mathrm{mW \cdot cm^{-2}}$ under different V_{ds}.

the dark current can be sustained post-illumination-this observation confirms the efficient electron transfer across the heterojunction. Specifically, electrons released from the defect states of 4H-SiC are continuously injected into the MoS_2 channel, enabling the device to maintain a relatively high initial dark current. Consistent with the results in Figure 3(f), an elevated V_{ds} leads to a higher steady-state current and a prolonged charge retention duration, which firmly validates the defect-enhanced non-radiative recombination effect.

Figure 4(a) is dedicated to explicitly demonstrating the multi-bit memory capability of the device: dynamic memory performance was characterized with a pulse width of 300 ms, yielding eleven distinguishable resistance states via ten consecutive light pulses. Meanwhile, Figure 4(b) shows that the device current exhibits a nonlinear response under continuous low-voltage stimulation. This characteristic stems from intrinsic defect-mediated trap states within the 4H-SiC lattice, manifesting as a dynamic behavior that first enhances and then saturates, which validates the feasibility of the device's multi-bit memory functionality. Such behavior mimics the core mechanism in biological neural learning, where synaptic efficacy is potentiated via iterative stimulation.

As shown in Figure 4(c), the device maintains a consistently upward current trend over multiple cyclic tests. This persistent current enhancement directly demonstrates the device's excellent operational stability and robust performance during repeated cycling, further validating the effectiveness of the SiC/MoS_2 heterostructure design in sustaining reliable functional performance.

Leveraging the ultra-low power consumption and exceptional performance of the SiC/MoS_2 heterostructure device, we further explore its application potential in neural network systems. Figure 4(d) depicts the neural network architecture for handwritten digit recognition [56], consisting of an input layer (784 neurons), a hidden layer (300 neurons), and an output layer (10 neurons). The MNIST recognition task is a hardware-calibrated software simulation based on conductance weight update data extracted from a single proof-of-concept device. Under ideal conditions (linear conductance, symmetric switching, negligible fluctuations), the simulated recognition accuracy depicted in Figure 4(e) reaches 86% in the first cycle and improves to 93.7% by the ninth cycle, which is only 2.3% below the ideal benchmark. During cyclic testing, the accuracy remains above 94%, closely matching the ideal curve and validating the excellent synaptic durability of the device under repeated potentiation and depression cycles.

In addition, to better illustrate the performance advantages of the present device, we perform a comparative analysis with a selection of representative synaptic devices. In general, the power consumption of these devices is determined using the equation [42]:

$$E = \int_0^T I_{\mathrm{d}} \times V \, \mathrm{d}t, \tag{3}$$

where I_{d}, V, and t represent the current response, bias voltage, and spike width, respectively.

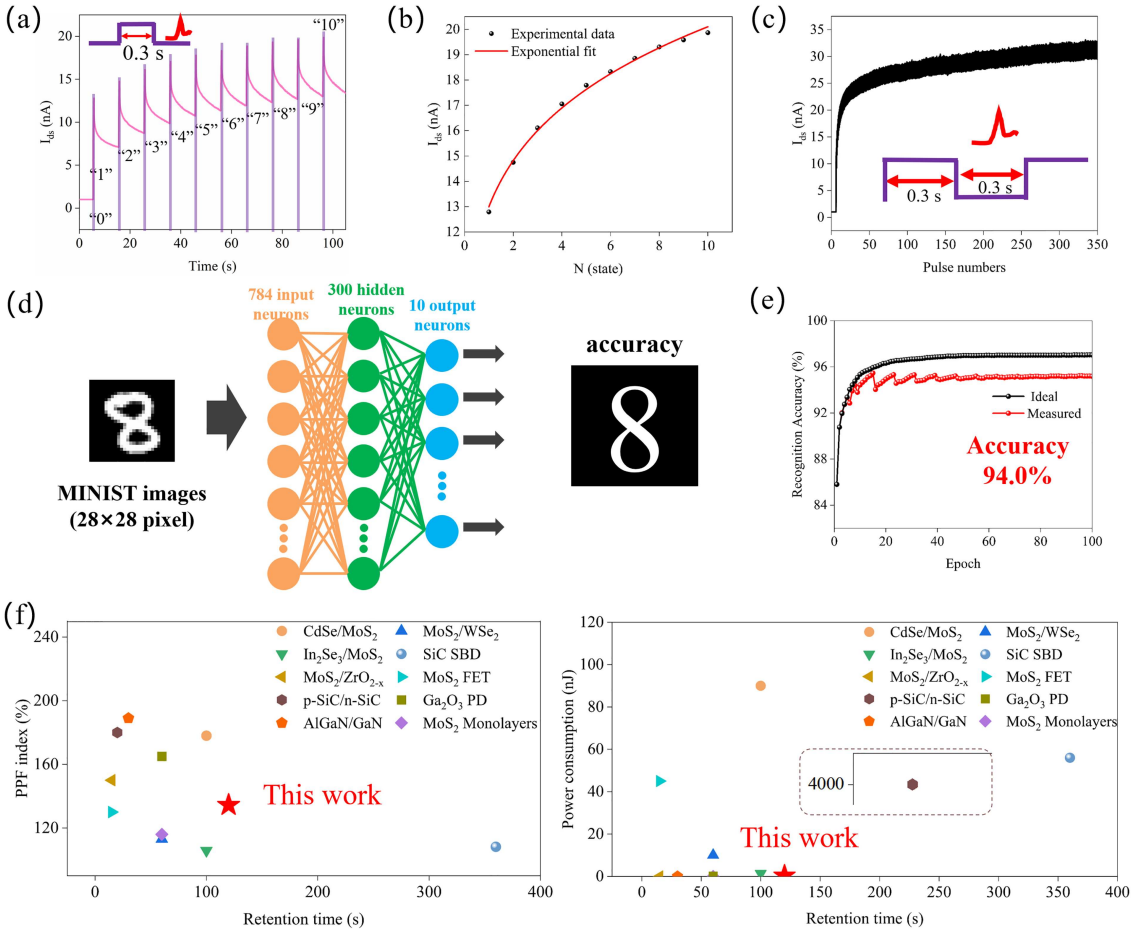

Figure 4 (Color online) (a) Multi-level storage achieved through continuous laser pulse stimulation at V_{ds} = 0.1 V; (b) the extracted I_{ds} of the discernible resistance states by ten consecutive photonic pulses; (c) current response to multiple optical pulses; (d) schematic illustration of the artificial neural network (ANN) to evaluate pattern recognition accuracy using a Modified National Institute of Standards and Technology (MNIST) data set; (e) image recognition accuracy of 100 trials for an idealized MoS_2/4H-SiC heterojunction device; (f) performance comparison diagram of PPF index, retention time, and power consumption with other classical devices [26, 47–55].

As shown in Figure 4(f), despite its excellent performance in terms of the PPF index, retention time, and power consumption, the fabricated device fails to maintain a competitive edge over other advanced devices across the entire spectrum of performance metrics. For instance, Table S1 presents key performance metrics of synaptic devices leveraging 2D materials, wide-bandgap materials, and heterojunctions, including retention time, PPF, and power consumption [26, 47–55]. The retention time of the device is inferior to that of previously reported SiC Schottky barrier diodes (SBDs) [55], yet it exhibits outstanding PPF and power consumption characteristics; conversely, its PPF and power consumption are not comparable to those of the Ga_2O_3 PD [48], whereas it demonstrates a distinct advantage in retention time.

In summary, the device has not yet achieved comprehensive advantages over state-of-the-art counterparts. Although the modulation of various bias voltages can effectively extend the retention duration, this strategy is accompanied by a simultaneous increase in power consumption, resulting in a critical trade-off that requires further mitigation. Nevertheless, while this SiC/MoS_2 heterostructure device serves as a promising candidate for the development of next-generation neuromorphic devices, several aspects still demand in-depth exploration and optimization. These include the modulation of material interfacial interactions, the precise tuning of intrinsic doping concentrations, and the integration of a gate structure to realize more sophisticated and flexible device control-all of which represent key directions for our future research.

Notably, the device features facile wafer-scale fabrication compatibility, which offers a versatile strategy for constructing wide-bandgap heterojunction-based artificial synapses. Such systems comprising large-area MoS_2/SiC heterojunction arrays directly integrated with field-programmable gate array (FPGA) hold great promise for future applications in extreme high-temperature neuromorphic computing and low-power edge intelligence sensing.

3 Conclusion

This study presents a photoelectric synaptic device based on a MoS_2/4H-SiC heterojunction, which systematically emulates information processing and synaptic plasticity mechanisms inherent to biological visual systems. By leveraging band engineering and interface regulation, the device achieves multi-parameter-tunable synaptic functionalities, including light power density-dependent current modulation and STP characteristics, such as pulse frequency- and pulse width-tunable synaptic weight potentiation.

Comprehensive characterizations via AFM, PL, ultraviolet photoelectron spectroscopy/valence band X-ray photoelectron spectroscopy (UPS/VB-XPS), and other techniques confirm that the heterojunction forms a type-I band alignment, highlighting the pivotal role of defect-mediated charge capture/release dynamics in realizing non-volatile storage.

Furthermore, neural networks constructed with this proof-of-concept device exhibit exceptional performance in handwritten digit recognition tasks: an initial recognition accuracy of 86% is achieved in the first cycle, with stability maintained above 94% over successive cyclic tests fully verifying the devices synaptic durability and operational reliability. This proof-of-concept platform offers a robust route for developing low-power, highly integrated neuromorphic computing and intelligent optoelectronic systems toward future wafer-scale implementation.

4 Experimental

Device fabrication. A 6-inch n-type SiC substrate, provided by Guangzhou Nansha Wafer Semiconductor Technology Co., Ltd., featured a 360 μm thickness (doping concentration of 3×10^{19} cm^{-3}) and a 11 μm epitaxial (doping concentration of 3×10^{15} cm^{-3}) layer. Following ultrasonic cleaning with anhydrous ethanol and acetone, a 100 nm silicon dioxide passivation layer was deposited on the substrate surface via plasma-enhanced chemical vapor deposition (PECVD, NAURA EPEE 550). Subsequently, the as-prepared substrate was spin-coated with a positive photoresist (ARP-5350, Taizhou SUNANO New Energy Co., Ltd.) at 3500 $r \cdot min^{-1}$ for 60 s and heated at 100°C for 4 min. The designed exposure pattern was obtained using a UV maskless photolithography machine (TuoTuo Technology, UV Litho-ACA) and a solution (AR 300-26, Taizhou SUNANO New Energy Co., Ltd.). Subsequently, the SiO_2/SiC sapphire substrate was rinsed in a buffer oxide etching (BOE) solution (NH_4F:HF = 6:1) for 60 s. Finally, the substrate was cleaned several times with acetone, ethanol, and deionized water. Moreover, several MoS_2 flakes were obtained on polydimethylsiloxane (PDMS) via mechanical exfoliation from bulk crystals (Shanghai Onway Technology Co., Ltd.). The chosen MoS_2 was in compact contact with the exposed SiC window and SiO_2 layer through a 3D microzone transfer platform (Shanghai Onway Technology Co., Ltd.). Finally, Cr/Au (10 nm/50 nm) electrodes were patterned and deposited using a UV maskless photolithography machine and an electron beam evaporation machine.

Characterization and measurement. Raman spectroscopy analysis was performed using a 532 nm laser confocal microscope; surface potential distribution was measured with a Bruker Dimension FastScan AFM; device optoelectronic performance characterization was completed using a three-probe station (Keithley 2636B) equipped with a light source. Photoresponse testing was conducted at 405 nm wavelength, with light power density calibrated using a PM400 power meter (Thorlabs). Steady-state PL spectra of SiC were acquired via a QE65000-FL fluorescence spectrometer; the material's energy level structure was determined using an UPS system (Thermo Nexsa).

Acknowledgements This work was supported by Financial Support from the Guangzhou S&T Programme (Grant No. 2025A04J1892), National Natural Science Foundation of China (Grant Nos. 62004071, 62375057), and Guangdong Basic and Applied Basic Research Foundation (Grant No. 2024A0505040026).

Supporting information Figures S1–S5, Note S1, and Table S1. The supporting information is available online at info.scichina.com and link.springer.com. The supporting materials are published as submitted, without typesetting or editing. The responsibility for scientific accuracy and content remains entirely with the authors.

References

1 Zhang Y, Qu P, Ji Y, et al. A system hierarchy for brain-inspired computing. Nature, 2020, 586: 378–384
2 Liu X Y, Gui Y S, Wang Z, et al. Robust optoelectronic dual-mode memristor enabled by ZnO/MoS_2 heterojunction for synaptic bionics and in-memory computing. Sci China Inf Sci, 2026, 69: 142405
3 Liu C, Chen H, Wang S, et al. Two-dimensional materials for next-generation computing technologies. Nat Nanotechnol, 2020, 15: 545–557
4 Zhu L, Li S X, Lin J C, et al. Ultra-low power IGZO optoelectronic synaptic transistors for neuromorphic computing. Sci China Inf Sci, 2024, 67: 222401
5 Liao F, Zhou Z, Kim B J, et al. Bioinspired in-sensor visual adaptation for accurate perception. Nat Electron, 2022, 5: 84–91
6 Li P, Shan X, Lin Y, et al. Tin doping induced high-performance solution-processed Ga_2O_3 photosensor toward neuromorphic visual system. Adv Funct Mater, 2023, 33: 2303584
7 Zidan M A, Jeong Y J, Lee J, et al. A general memristor-based partial differential equation solver. Nat Electron, 2018, 1: 411–420

8 Zhao Z, Hu Z, Deng M, et al. Bias-switchable photodetection and photosynapse dual-functional devices based on 2D perovskite/organic heterojunction for imaging-to-recognition conversion. Adv Mater, 2024, 37: 2416033
9 Kim G, Yoo D, So H, et al. Precise weight tuning in quantum dot-based resistive-switching memory for neuromorphic systems. Mater Horiz, 2025, 12: 915–925
10 Zhao R, Wu H, Gao K, et al. Synergistic breakthrough in speed and power: TiO_2/SiO_2 stacked dielectric heterostructures for phase-change memory. ACS Appl Mater Interfaces, 2025, 17: 48849–48854
11 Mulaosmanovic H, Muller S, Noack M, et al. Novel ferroelectric FET based synapse for neuromorphic systems. In: Proceedings of the 2017 Symposium on VLSI Technology, Kyoto, 2017. 176–177
12 Hong S, Cho H, Kang B H, et al. Neuromorphic active pixel image sensor array for visual memory. ACS Nano, 2021, 15: 15362–15370
13 Huang X, Li Q, Shi W, et al. Dual-mode learning of ambipolar synaptic phototransistor based on 2D perovskite/organic heterojunction for flexible color recognizable visual system. Small, 2021, 17: 2102820
14 Zeng S, Tang Z, Liu C, et al. Electronics based on two-dimensional materials: status and outlook. Nano Res, 2020, 14: 1752–1767
15 Zhang Y, Tang Y, Liu K, et al. Optoelectronic synapse based on Te/SnS_2 heterostructure with integrated sensing-memory-computing for neuromorphic visual system. Adv Opt Mater, 2025, 13: 2501371
16 Xue F, He X, Liu W, et al. Optoelectronic ferroelectric domain-wall memories made from a single van der Waals ferroelectric. Adv Funct Mater, 2020, 30: 2004206
17 Ci W, Xue W, Wang P, et al. All-in-one optoelectronic neuristor based on full-vdW two-terminal ferroelectric p-n heterojunction. Adv Funct Mater, 2023, 34: 2305822
18 Han W, Zheng X, Yang K, et al. Phase-controllable large-area two-dimensional In_2Se_3 and ferroelectric heterophase junction. Nat Nanotechnol, 2022, 18: 55–63
19 Fu Y, Huang Y, Huang Q, et al. Gradient pyrolysis-derived multiphase heterogeneous interfaces for enhanced electromagnetic wave absorption. Carbon, 2026, 247: 121013
20 Chen H, Shao C, Li X, et al. Self-powered epitaxial graphene/SiC-C heterojunction UV photodetector. Sens Actuat A-Phys, 2024, 376: 115604
21 Jehad A K, Fidan M, Ünverdi Ö, et al. CVD graphene/SiC UV photodetector with enhanced spectral responsivity and response speed. Sens Actuat A-Phys, 2023, 355: 114309
22 Fu Z, Liu J, Yuan M, et al. Local avalanche photodetectors driven by lightning-rod effect and surface plasmon excitations. Nat Commun, 2025, 17: 76
23 Lin L, Huo J, Peng P, et al. Contact engineering of single core/shell SiC/SiO_2 nanowire memory unit with high current tolerance using focused femtosecond laser irradiation. Nanoscale, 2020, 12: 5618–5626
24 Kapur O, Guo D, Reynolds J, et al. Back-end-of-line SiC-based memristor for resistive memory and artificial synapse. Adv Elect Mater, 2022, 8: 2200312
25 Shen W, Wang P, Wei G, et al. SiC@NiO core-shell nanowire networks-based optoelectronic synapses for neuromorphic computing and visual systems at high temperature. Small, 2024, 20: 2400458
26 Liu X, Shi Z, Bu M, et al. 4H-SiC homojunction photogated synapses enabling high-temperature neuromorphic computing. Small, 2025, 21: 2504084
27 Ren J, Shen H, Liu Z, et al. Artificial synapses based on WSe_2 homojunction via vacancy migration. ACS Appl Mater Interfaces, 2022, 14: 21141–21149
28 Islam M M, Krishnaprasad A, Dev D, et al. Multiwavelength optoelectronic synapse with 2D materials for mixed-color pattern recognition. ACS Nano, 2022, 16: 10188–10198
29 Zhang Z, Zhao X, Zhang X, et al. In-sensor reservoir computing system for latent fingerprint recognition with deep ultraviolet photo-synapses and memristor array. Nat Commun, 2022, 13: 6590
30 Gao W, Zhang F, Zheng Z, et al. Unique and tunable photodetecting performance for two-dimensional layered $MoSe_2/WSe_2$ p-n junction on the 4H-SiC substrate. ACS Appl Mater Interfaces, 2019, 11: 19277–19285
31 Jiang Y, Zhang L, Wang R, et al. Asymmetric ferroelectric-gated two-dimensional transistor integrating self-rectifying photoelectric memory and artificial synapse. ACS Nano, 2022, 16: 11218–11226
32 Aldalbahi A, Li E, Rivera M, et al. A new approach for fabrications of SiC based photodetectors. Sci Rep, 2016, 6: 23457
33 Fujisawa K, Carvalho B R, Zhang T, et al. Quantification and healing of defects in atomically thin molybdenum disulfide: beyond the controlled creation of atomic defects. ACS Nano, 2021, 15: 9658–9669
34 Fabbri F, Cavalcoli D, Cavallini A. 4H-SiC band structure investigated by surface photovoltage spectroscopy. Acta Mater, 2012, 60: 3350–3354
35 Lu W, Tarekegne A T, Ou Y, et al. Temperature-dependent photoluminescence properties of porous fluorescent SiC. Sci Rep, 2019, 9: 16333
36 Li R, Wang W, Li Y, et al. Multi-modulated optoelectronic memristor based on Ga_2O_3/MoS_2 heterojunction for bionic synapses and artificial visual system. Nano Energy, 2023, 111: 108398
37 Guo J, Liu L, Wang J, et al. A diffusive artificial synapse based on charged metal nanoparticles. Nano Lett, 2024, 24: 1951–1958
38 Qiu D, Zheng S, Hou P. Simulating and implementing broadband van der Waals artificial visual synapses based on photoconductivity and pyroconductivity mechanisms. ACS Appl Mater Interfaces, 2024, 16: 53142–53152
39 Park K, Kang B H, An J B, et al. Endurable IGZO/SnS_x/IGZO heterojunction phototransistor arrays for image sensors. ACS Appl Mater Interfaces, 2025, 17: 3620–3630
40 Li L, Wei G, Zhu P, et al. Self-powered solar-blind photodetector with low dark current and ultrahigh on/off ratio based on vertically aligned Si/SiC nanowire arrays p-n heterojunction. IEEE Trans Electron Devices, 2024, 71: 4173–4179
41 Brodar T, Bakrač L, Capan I, et al. Depth profile analysis of deep level defects in 4H-SiC introduced by radiation. Crystals, 2020, 10: 845–860
42 Chen C, Zhou Y, Tong L, et al. Emerging 2D ferroelectric devices for in-sensor and in-memory computing. Adv Mater, 2024, 37: 2400332
43 Ren X, He X, Duan Z, et al. Self-powered and broadband optical synapse device based on Se-vacancy Bi_2O_2Se for artificial vision system application. ACS Photonics, 2024, 11: 4990–4999
44 Kawahara K, Thang Trinh X, Tien Son N, et al. Quantitative comparison between $Z_{1/2}$ center and carbon vacancy in 4H-SiC. J Appl Phys, 2014, 115: 143705
45 Zhou Y, Li F, Li W, et al. MoS_2/GaN junction field-effect transistors with ultralow subthreshold swing and high on/off ratio via thickness engineering for logic inverters. Adv Funct Mater, 2024, 34: 2410954
46 Lian Z, Wei J, Liu Y, et al. Highly responsive dual-function deep-ultraviolet neuromorphic phototransistors based on silicon carbide nanoparticle/2D MoS_2 heterostructures. ACS Nano, 2025, 19: 26041–26054
47 Song X, Lv X, He M, et al. Artificial optoelectronic synapse based on CdSe nanobelt photosensitized MoS_2 transistor with long retention time for neuromorphic application. Nanophotonics, 2024, 13: 4211–4224
48 Sun H, Ye B, Ge M, et al. Artificial optoelectronic synapses based on Ga_2O_3 metal-semiconductor-metal solar-blind ultraviolet photodetectors with asymmetric electrodes for neuromorphic computing. Responsive Mater, 2025, 3: 20240038
49 Hu Y, Yang H, Huang J, et al. Flexible optical synapses based on In_2Se_3/MoS_2 heterojunctions for artificial vision systems in the near-infrared range. ACS Appl Mater Interfaces, 2022, 14: 55839–55849
50 Jang H Y, Kwon O, Nam J H, et al. Highly reproducible heterosynaptic plasticity enabled by MoS_2/ZrO_{2-x} heterostructure memtransistor. ACS Appl Mater Interfaces, 2022, 14: 52173–52181

51 Wang B, Zhang Y, You J, et al. An image detection-memory-recognition artificial visual unit based on dual-gate phototransistors. Adv Intelligent Syst, 2023, 5: 2200328
52 Huang M, Ali W, Yang L, et al. Multifunctional optoelectronic synapses based on arrayed MoS_2 monolayers emulating human association memory. Adv Sci, 2023, 10: 2300120
53 Li X, Sun H, Ge M, et al. Optically tunable synaptic transistors based on AlGaN/GaN heterostructure for neuromorphic vision processing. Appl Phys Lett, 2025, 127: 213301
54 You J, Wang L, Zhang Y, et al. Simulating tactile and visual multisensory behaviour in humans based on an MoS_2 field effect transistor. Nano Res, 2023, 16: 7405–7412
55 Zhang G, Liu W, Huo N, et al. Vertical monolithic SiC optoelectronic synapses with visible-light neuromorphic plasticity. ACS Appl Electron Mater, 2025, 7: 6560–6569
56 Fuller E J, Gabaly F E, Léonard F, et al. Li-ion synaptic transistor for low power analog computing. Adv Mater, 2016, 29: 1604310